




Stress-Induced Transformations of Polarization Switching in CuInP_2S_6 Nanoparticles

Anna N. Morozovska ^{1,*} Eugene A. Eliseev ² Mykola E. Yelisieiev ³
Yulian M. Vysochanskii ^{4,†} and Dean R. Evans^{5,‡}

¹*Institute of Physics, National Academy of Sciences of Ukraine, Nauky Avenue, Bldg. 46, Kyiv 03028, Ukraine*

²*Institute for Problems of Materials Science, National Academy of Sciences of Ukraine, Krjijanovskogo Street, Bldg. 3, Kyiv 03142, Ukraine*

³*Physics Faculty of Taras Shevchenko National University of Kyiv, Volodymyrska Street 64, Kyiv 01601, Ukraine*

⁴*Institute of Solid State Physics and Chemistry, Uzhhorod University, Uzhhorod 88000, Ukraine*

⁵*Materials and Manufacturing Directorate, Air Force Research Laboratory, Wright-Patterson Air Force Base, Ohio 45433, USA*



(Received 20 February 2023; revised 27 April 2023; accepted 28 April 2023; published 25 May 2023)

Using the Landau-Ginzburg-Devonshire approach, we study stress-induced transformations of polarization switching in ferroelectric CuInP_2S_6 nanoparticles for three different shapes: a disk, a sphere, and a needle. Semiconducting properties of a nanoparticle are modeled by a surface-charge layer, whose effective screening length can be rather small due to the field effect. We reveal a very strong and unusual influence of hydrostatic pressure on the appearance of polarization switching in CuInP_2S_6 nanoparticles, hysteresis loop shape, magnitude of the remanent polarization, and coercive fields, and explain the effects by the anomalous temperature dependence and “inverted” signs of CuInP_2S_6 linear and nonlinear electrostriction coupling coefficients. In particular, by varying the sign of the applied pressure (from tension to compression) and its magnitude (from zero to several hundreds of MPa), quasistatic hysteresisless paraelectric curves can transform into double, triple, pinched, or single hysteresis loops. Unexpectedly, we predict that stressed CuInP_2S_6 nanospheres and nanoneedles reveal sizeable temperature and pressure ranges of triple loop stability, which are very rare in ferroelectrics and antiferroelectrics. A physical origin of triple loops is the coexistence of “small” and “larger” polarizations in the four-well ferroelectric state. Due to the sufficiently wide temperature and pressure ranges of double, triple, and pinched hysteresis loop stability (at least in comparison with many other ferroelectrics), CuInP_2S_6 nanodisks can be of particular interest for applications in energy storage (in the region of double loops), CuInP_2S_6 nanospheres maybe suitable for dynamic random-access multibit memory, and CuInP_2S_6 nanoneedles are promising for nonvolatile multibit memory cells (in the regions of triple and pinched loops). The stress control of the polarization-switching scenario allows the creation of advanced piezosensors based on CuInP_2S_6 nanocomposites.

DOI: [10.1103/PhysRevApplied.19.054083](https://doi.org/10.1103/PhysRevApplied.19.054083)

I. INTRODUCTION

Room-temperature uniaxial low-dimensional ferroics are very promising for advanced nanoscale nonvolatile memory cells, information, and energy storage [1]. The feasible control of polarization switching by external stress, strain, or their gradients is especially useful to improve the memory performances of ferroics. That is why the stress-induced phase transitions [2] and strain engineering [3,4] become especially relevant in nanoparticles

and ultrathin films of Cu-based layered chalcogenides, $\text{CuInP}_2(\text{S}, \text{Se})_6$ [5–7]; these materials are uniaxial ferroics [8–10], whose value for advanced applications is due to a possibility of the ferroelectricity, ferrielectricity, and anti-ferrielectricity downscaling to the limit of a single layer [11,12]. Ferrielectricity, the equivalent of ferrimagnetism, can be termed as an antiferroelectric order, but with a switchable spontaneous polarization created by two sublattices with spontaneous dipole moments that are antiparallel and different in magnitude [13]. In accordance with this definition and experimental results [14,15], $\text{CuInP}_2(\text{S}, \text{Se})_6$ should be considered as a ferrielectric material, because it has two polar sublattices, Cu and In, whose electric dipole moments are antiparallel and different in magnitude

*anna.n.morozovska@gmail.com

†vysochanskii@gmail.com

‡dean.evans@afrl.af.mil

in the absence of external electric field and applied pressure. Note, that the *ab initio* calculations [12] show that the ferroelectric state can be achieved in CuInP_2S_6 and CuCrP_2S_6 during polarization switching, but the state is metastable. More recent *ab initio* calculations [16] reveal that lattice anharmonicity effects stabilize the ferroelectric state in CuInP_2S_6 .

Despite the significant fundamental and practical interest in bulk [14] and nanosized $\text{CuInP}_2(\text{S},\text{Se})_6$ [17], the influence of stress and strains on the switching of its spontaneous polarization has been very poorly studied from a theoretical perspective. There are a few mostly experimental works considering polarization switching in $\text{CuInP}_2(\text{S},\text{Se})_6$ ultrathin films and nanoflakes (see, e.g., Refs. [3,4] and references therein).

The spontaneous polarization of crystalline CuInP_2S_6 (CIPS) is directed normally to its structural layers as a result of antiparallel shifts of the Cu^+ and In^{3+} cations from the middle of the layers [5,14,17]. Acentric positions of Cu^+ cations in the surrounding sulfur atoms' octahedra are determined by the second-order Jahn-Teller (SOJT) effect, which determines their two-well local potential with the Cu^{up} and Cu^{down} positions of the copper atoms in the ground state. The Cu^+ cations flip between Cu^{up} and Cu^{down} positions with a temperature increase and populate the positions with equal probability above the temperature of the structural transition from the polar ferroelectric (FI) to the nonpolar paraelectric (PE) phase. Complementary to the sublattice of the Cu^+ cations, the sublattice of In^{3+} cations also play a role in the polar ordering of the CIPS crystal lattice. The indium cations with $4d^{10}3s^0p^0$ electronic configuration have some degree of covalence of their chemical bonding with the nearest sulfur atoms, which is determined by sp^2 hybridization because of their stereochemical activity, and form the three-well local potential with a stable central well and two metastable side wells [17]. The local potential determines the shift of the indium cations, which is opposite to the deviation of copper cations from the middle of CIPS structural layers.

Using pseudospin formalism, the polar ordering of CIPS can be described in the Ising model with spins $s = \frac{1}{2}$ and $S = 1$ [18], and a mixed anisotropy of the local crystal field. Within the model, the spins \vec{s} with projections $+\frac{1}{2}$ and $-\frac{1}{2}$ can be associated with the local dipoles induced by Cu^+ cations and P_2S_6 anion complexes, and spins \vec{S} with projections $+1, 0, -1$ can be related with the local dipoles induced by In^{3+} cations and P_2S_6 anion complexes. In the mean-field approximation [19,20], the presence of two types of cationic sublattices in ferroelectrics is described by polar (dipolar) and antipolar (nonpolar) order parameters, P and A , respectively. They formally correspond to projections $\vec{S} = \pm 1$ (in the polar state) and $\vec{S} = 0$ (in the nonpolar state) in the pseudospin formalism. As a rule, the polar-order parameter is observable (i.e., measurable), and the antipolar-order parameter cannot

be directly measured. Indirectly, the nonlinear coupling between A and P increases the order of the thermodynamic potential up to the eight power (see Appendix A in Ref. [20] for details). Using the eight-power thermodynamic potential [2] in this case, we predict a temperature-pressure phase diagram [20], containing the critical end point (CEP) where the first-order PE-FI phase transition line terminates, and the bicritical end point (BEP) where the first-order isostructural phase transition line between two ferroelectric states (FI1 and FI2) with different amplitudes of spontaneous polarization terminates.

Using the eight-power free-energy functional of polarization, Ishibashi and Hidaka [21] analyzed the phase diagram in a two-sublattice model with an asymmetric double-well potential. They calculate a phase diagram containing a triple point (analog of the CEP), an end point (analog of the BEP), and an isomorphous first-order phase transition line between the triple point and the end point embedded in a polar region (analog of the first-order isostructural transition between the FI2 and FI1 states in Ref. [20]). Their Kittel-type model considers polar- (P) and antipolar- (A) order parameters, expressed via the sublattices' polarizations P_1 and P_2 , as $P = (P_1 + P_2)/2$ and $A = (P_1 - P_2)/2$, and includes a bilinear intersublattice coupling term, gP_1P_2 . Ishibashi and Hidaka did not consider a switching of the spontaneous polarization.

Using the sixth-power and fourth-power free-energy functional of polarization, Iwata and Ishibashi [22] consider the polarization switching in the first-order ferroelectrics and second-order antiferroelectrics, and found double hysteresis loops of polarization switching in a narrow temperature range above the Curie temperature (i.e., inside the PE phase). Toledano and Guennou [13] analyzed electric field-induced antiferroelectric-ferrielectric-ferroelectric transitions in the frame of the Kittel model with sixth-order invariants in P and in the presence of nonlinear coupling between A and P . They defined the range of model parameters required for the appearance of double hysteresis loops. Balashova and Tagantsev [23] considered the fourth-power free-energy functional of a ferroic with a nonlinear coupling between the structural-order parameter and the polarization, and revealed the existence of double hysteresis loops in the system. Recently, Lum *et al.* [24] developed the Kittel model by considering sixth-order invariants and bilinear coupling between dipolar sublattices, and observed double hysteresis loops of polarization switching. Double and pinched hysteresis loops were observed in uniaxial ferroelectrics and were explained with the axial next nearest-neighbor Ising (ANNNI) model by Zamaraita *et al.* [25]. An early paper by Suzuki and Okada [26], which developed the Kittel model by taking the sixth-order invariants, bilinear, and biquadratic nonlinear coupling terms, gP_1P_2 and $h(P_1P_2)^2$, described the phase diagram with paraelectric, polar (ferroelectric), semipolar (ferrielectric), and antipolar (antiferroelectric) phases.

They predicted “anomalous” triple loops in the semipolar phase. It was mentioned, that the triple loops can be smeared at the rise of the coercive electric fields, because of the enhanced hysteresis effect. Pinched and triple loops were predicted in multiaxial ferroelectrics [27], and their significance for the creation of “symmetry-protected” ferroelectric multibit memory-cell concept was revealed by Baudry *et al.* [27] and Mangeri *et al.* [28].

Using the eighth-order Landau-Ginzburg-Devonshire (LGD) thermodynamic potential [2,20] and finite-element modeling (FEM), we study the stress-induced transformations of polarization switching in CIPS nanoparticles, whose shape varies, i.e., a prolate needle, an oblate disk, or a sphere. Much attention is paid to the analysis of the correlations between the peculiarities of spontaneous polarization switching by an electric field and the topology of the temperature-pressure phase diagram. We reveal relatively wide temperature and pressure ranges of double, triple, and pinched hysteresis loop stability (at least in comparison with many other ferroelectrics).

The original part of this work contains the physical description of the problem and LGD approach (Sec. II), considers in detail the stress-induced transformations of a polarization-switching scenario and hysteresis loop changes in the nanoparticles (Secs. III A and III B), and discusses possible applications of stressed CIPS nanoparticles in multibit memory cells (in the region of pinched and triple loops) and energy storage (in the region of double loops). Section IV provides conclusions of the results. Supplemental Material contain a mathematical formulation of the problem, a table of material parameters, a description of methods, and numerical algorithms.

II. PROBLEM FORMULATION

A CIPS nanoparticle, whose shape can be spherical, prolate ellipsoidal, or oblate ellipsoidal, is schematically shown in Figs. 1(a)–1(c), respectively. The spontaneous polarization, P_s , is directed along the CIPS polar axis “ X_3 ,” which coincides with the ellipsoid semiaxis L . Two other semiaxes in X_1 and X_2 directions are equal to R . As a matter of fact, P_s is the total polarization of four possible polar-active sublattices (see Fig. 1 in Ref. [20]) in which individual dipole moments of the four Cu and four In atoms are antiparallel and different in magnitude in the absence of an external electric field and an applied pressure. The polarization can be determined from standard electrical measurements of the nanocomposite capacitance (e.g., as a remanent polarization of the hysteresis loop), as well as estimated by piezoelectric response microscopy of separated nanoflakes.

To analyze the polarization-field dependence, $P_3(E_0)$, we consider a nanoparticle placed in a homogeneous quasistatic electric field \vec{E}_0 co-directed with its polar axis. The electric field \vec{E} existing inside the nanoparticle is a superposition of the external \vec{E}_0 and the depolarization \vec{E}_d fields created by the uncompensated bound charges (ferroelectric dipoles) near the particle surface and domain walls (if any exist).

Let us consider a CIPS nanoparticle placed in ambient conditions. In what follows we assume that the depolarization field is partially screened by the surface charge with density ρ_s that covers the nanoparticle “core” as a screening “shell.” The physical nature of the surface charge determines the dependence of ρ_s on the acting electric field [29]. In what follows we account for the fact

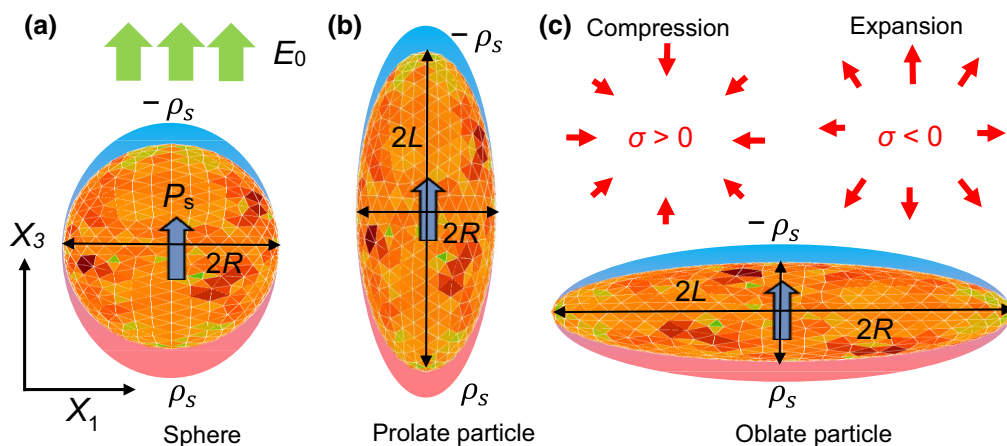


FIG. 1. A CIPS nanoparticle whose shape can be spherical (a) with radius R , prolate ellipsoidal (b), or oblate ellipsoidal (c) with semiaxes R and L . Mesh elements, used in FEM, are shown by light-green, orange, red, and dark-red colors. The shell of surface charge with density ρ_s covers the nanoparticle core. The thick blue arrow shows the spontaneous polarization P_s , directed along the axis X_3 ; thinner red arrows illustrate the direction of the hydrostatic pressure application (compression, $\sigma > 0$, or expansion, $\sigma < 0$). The $\{X_1-X_3\}$ cross section of 3D ellipsoids is shown.

that an effective screening length, λ , associated with the density, ρ_s , is strongly field dependent in semiconductors, such as CIPS. It is the consequence of the depolarization field effect in ferroelectrics-semiconductors that causes the band bending near their surface. The band-bending effect is weak for a small E_0 , and therefore the density of free charges induced by E_0 is relatively small inside the core. At the same time, the “bare” (i.e., unscreened) depolarization field, \vec{E}_d , significantly exceeds the thermodynamic coercive field near the core surface. Strong band bending occurs in response to this bare field, and as a result the field-induced density of the screening charge becomes very high at the core surface, which decreases E_d in a self-consistent way. Since the charge density determines the value of λ , hereinafter we take into account that λ is significantly different for the external and depolarizing fields, namely $\lambda(E_0) \gg \lambda(E_d)$.

It has been shown in Refs. [2,19,20] that the density of the LGD free energy of CIPS has four potential wells at $\vec{E} = 0$. The free-energy density includes the Landau-Devonshire expansion in even powers of the polarization P_3 (up to the eighth power), the Ginzburg gradient energy, and the elastic and electrostriction energies, which are listed in Appendix A within the Supplemental Material [30]. Polarization dynamics in an external field follows from the time-dependent LGD equation, which in turn follows from the minimization of the LGD free energy, and has the form:

$$\Gamma \frac{\partial P_3}{\partial t} + [\alpha - 2\sigma_i(Q_{i3} + W_{ij3}\sigma_j)]P_3 + (\beta - 4Z_{i33}\sigma_i)P_3^3 + \gamma P_3^5 + \delta P_3^7 - g_{33kl} \frac{\partial^2 P_3}{\partial x_k \partial x_l} = E_3. \quad (1)$$

Γ is the Khalatnikov kinetic coefficient [31]. The coefficient α depends linearly on the temperature T , $\alpha(T) = \alpha_T(T - T_C)$, where T_C is the Curie temperature of a bulk ferroelectric. The coefficients β , γ , and δ in Eq. (1) are temperature independent. The values σ_i denote diagonal components of a stress tensor in the Voigt notation, and the subscripts $i, j = 1 - 6$. The values Q_{i3} , Z_{i33} , and W_{ij3} denote the components of a single linear and two nonlinear electrostriction strain tensors in the Voigt notation, respectively [32,33]. The values g_{33kl} are polarization gradient coefficients in the matrix notation and the subscripts $k, l = 1 - 3$. The boundary condition for P_3 at the nanoparticle surface S is “natural”, i.e., $g_{33kl}n_k(\partial P_3/\partial x_l)|_S = 0$, where \vec{n} is the outer normal to the surface.

The value E_3 is an electric field component co-directed with the polarization P_3 , which is a superposition of external and depolarization fields. In order to analyze a quasistatic polarization reversal, we assume that the period, $2\pi/\omega$, of the sinusoidal external field is very small in comparison with the Landau-Khalatnikov relaxation time,

$\tau = \Gamma/|\alpha|$. The quasistatic field E_3 is related to the electric potential ϕ as $E_3 = -(\partial\phi/\partial x_3)$. The electric potential ϕ satisfies the Poisson equation inside the particle core,

$$\varepsilon_0 \varepsilon_b \Delta \phi = \frac{\partial P_3}{\partial x_3}. \quad (2)$$

The Laplace equation outside the screening shell is $\Delta\phi = 0$. The three-dimensional (3D) Laplace operator is denoted by the symbol Δ . Parameters ε_0 and ε_b are the universal dielectric constant and the background dielectric permittivity [34] of the ferroelectric core, respectively. Equation (2) is supplemented by the condition of potential continuity at the particle surface, $(\phi_{\text{ext}} - \phi_{\text{int}})|_S = 0$. The boundary condition for the normal components of the electric displacement \vec{D} is $\vec{n}(\vec{D}_{\text{ext}} - \vec{D}_{\text{int}})|_S = \rho_s$, where the surface-charge density $\rho_s = -\varepsilon_0\phi/\lambda$ and λ is the above-mentioned effective screening length.

The values of T_C , α_T , β , γ , δ , Q_{i3} , W_{ij3} , and Z_{i33} have been determined in Refs. [2,19,20] from the fitting of temperature-dependent experimental data for the dielectric permittivity [35–37], spontaneous polarization [14,38], and lattice constants [10] as a function of hydrostatic pressure. Elastic compliances s_{ij} are calculated from ultrasound velocity measurements [39,40]. The gradient coefficients g_{33ij} are estimated from the width of domain walls. The CIPS parameters used in our calculations are listed in Table SI, Appendix A within the Supplemental Material [30].

Due to the strong, negative, and temperature-dependent nonlinear electrostriction coupling coefficients (namely $Z_{i33} < 0$ and $W_{ij3} < 0$), and the “inverted” signs of the linear electrostriction coupling coefficients (namely $Q_{33} < 0$, $Q_{23} > 0$, and $Q_{13} > 0$) for CIPS, the expected pressure effect on the polarization switching is complex and unusual in comparison with many ferroelectrics where $Q_{33} > 0$, $Q_{23} < 0$, and $Q_{13} < 0$ [2]. We also want to underline that below we consider only hydrostatic pressure, $\sigma_1 = \sigma_2 = \sigma_3 = -\sigma$, since the case is the easiest to realize experimentally for an ensemble of nanoparticles. Note that the surface tension can renormalize the stresses as $\sigma_1 = -\sigma - (\mu/R)$, $\sigma_2 = -\sigma - (\mu/R)$, and $\sigma_3 = -\sigma - (\mu/L)$ [41], where $\mu \cong (1 - 3) \text{ N/m}$ is a relatively small surface-tension coefficient [42,43]. In order to focus on the influence of external pressure, we mostly neglect the surface tension in this work.

III. STRESS-INDUCED TRANSFORMATIONS OF POLARIZATION SWITCHING

A. Finite-element modeling of a polarization switching

We perform FEM in COMSOL Multiphysics software using electrostatics, solid mechanics, and general math (PDE toolbox) modules. FEM is performed for different nanoparticle sizes and shapes, discretization densities of

the self-adaptive tetragonal mesh, and initial polarization distributions (e.g., randomly small fluctuations or polydomain states) and their relaxation conditions (see details in Appendix A within the Supplemental Material [30]). Examples of mesh elements used in FEM are shown in Fig. 1. The smallest elements have a light-green color, larger elements are orange and red, and the largest have a dark-red color.

Typical quasistatic hysteresis loops, $P_3(E)$, calculated for a stress-free CIPS nanoparticle with radius $R = 6$ nm at 293 K, are shown in Fig. 2(a). The loop shape strongly depends on the amplitude V_0 of the applied voltage (compare black, blue, red, and green loops). Figure 2(a) also

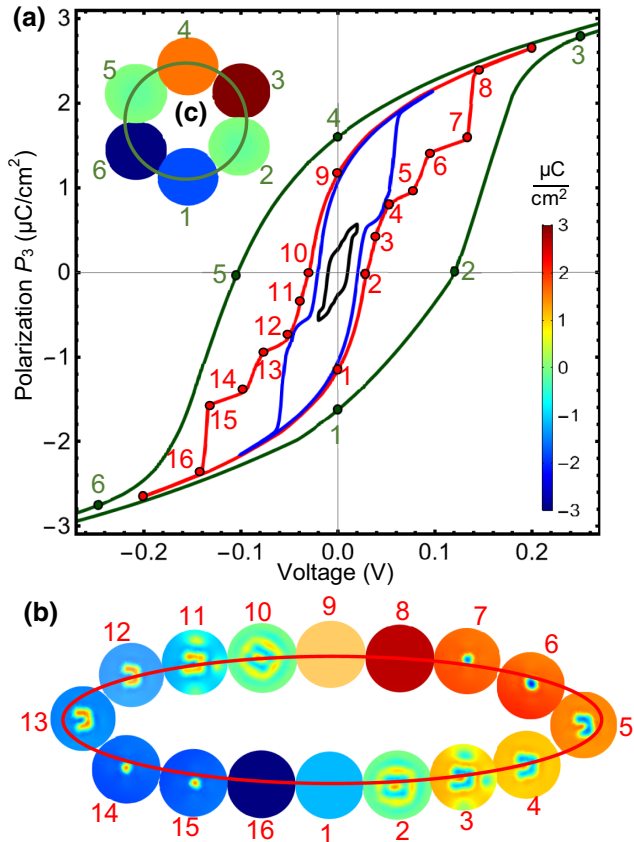


FIG. 2. (a) Hysteresis loops, $P_3(E)$, calculated for a stress-free CIPS nanoparticle at different amplitudes of applied voltage: 0.02 V (black loop), 0.1 V (blue loop), 0.2 V (red loop), and 2 V (dark-green loop). Color images (b),(c) are the polarization distribution in the equatorial cross section of the particle perpendicular to its polar axis. Color images 2–7 and 10–15 in the plot (b) are the polydomain polarization states in the corresponding points on the red loop; and images 1, 8, 9, and 16 are the single-domain polarization states on the red loop. Color images 1–6 in the plot (c) are the single-domain polarization states in points 1–6 on the dark-green loop. The color scale is the value of electric polarization in $\mu\text{C}/\text{cm}^2$. Nanoparticle radius $R = 6$ nm, $\lambda = 0.1$ nm, $T = 293$ K, and $\mu = 0$; CIPS parameters are listed in Table SI within the Supplemental Material [30].

shows that the polarization switching is mostly polydomain for a small V_0 value, and the corresponding loop has an unsaturated rhomblike shape with small vertical steps (see black loop calculated for $V_0 = 0.02$ V). The total amount of domain walls and the fraction of polydomain states decrease with an increase in V_0 , where the loop shape becomes more saturated and the vertical steps become much more pronounced (compare blue and red loops calculated for $V_0 = 0.1$ V and 0.2 V, respectively). Each step corresponds to a sharp change or “rebuilding” of the domain structure inside the nanoparticle. This rebuilding occurs at some critical voltage, as shown in the images 1–16 in Fig. 2(b), which corresponds to the partially polydomain polarization switching in the red loop calculated for $V_0 = 0.2$ V. The sharp changes of the domain structure morphology mimic Barkhausen jumps [44] observed experimentally during the polarization reversal in many ferroelectrics. However, there are several principal differences between steps and Barkhausen jumps. For a specified particle size and temperature, the steps’ position and height do not depend on the initial polarization distribution (i.e., on the sample prehistory) nor the number of voltage cycles; but it does depend on the average size and shape of mesh elements. We regard that Marton’s finding [45] can explain the possible origin of the coercive and critical fields’ dependence on the discretization by appearance of Peierls-Nabarro-type barriers in simulations. In contrast, Barkhausen jumps are determined by domain walls pinning by defects, and, as a rule, they become less visible or disappear after multiple voltage cycles.

It is interesting that the polydomain polarization states, shown in Fig. 2(b), appear for a range of voltages when the voltage is increasing (see, e.g., points 2–8), but they are absent for the same magnitude of voltage when the voltage is decreasing (see, e.g., points 8–10). This is because once the applied field has created a stable single-domain state, it persists as a metastable state when the voltage is lowered from the maximal value to coercive value (e.g., to the point 10). Only below the coercive voltage is the metastable state destroyed by the electric field and the domain nucleation appears (see, e.g., points 11–16).

The polarization switching scenario exhibits a single-domain structure with a further increase of V_0 , and the hysteresis loop acquires a saturated shape without any steps (see the dark-green loop calculated for $V_0 = 2$ V). The corresponding polarization distribution is quasiuniform for the entire loop [see color images 1–6 in the plot Fig. 2(c)]. The coercive voltage corresponding to the dark-green loop (approximately 0.14 V) is significantly higher than the coercive voltages corresponding to other loops (approximately 0.01–0.02 V) in Fig. 2(a). This is because a single-domain polarization switching occurs at the thermodynamic coercive field, which is significantly higher than the critical fields of domain-wall motion. The shape of the

single-domain loop is defined by the structure of the LGD potential only.

As it has been shown earlier [46], the domain structure appearance and its morphology in the ferroelectric state, as well as the critical sizes of the CIPS core corresponding to the FI-PE phase transition, depend strongly on the magnitude and anisotropy of the polarization gradient coefficients, g_{33ij} [see Eq. (1)]. In particular, a small increase in g_{33ij} (e.g., above 10^{-9} J m³/C²) leads to a relatively small increase of the critical sizes (less than several nm), but it strongly suppresses the domain-structure appearance in the FI state. For instance, in the case $g \cong 2 \times 10^{-9}$ J m³/C² (used in this work, see Table SI in the Supplemental Material [30]) and $\lambda = (0.1 - 0.5)$ nm, CIPS nanoparticles are mostly single-domain above the critical sizes (approximately 5 nm) and PE below the critical sizes. Furthermore, for the case of natural boundary conditions used in this work, $g_{33ij} n_i (\partial P_3 / \partial x_j) = 0$, polarization gradient effects can be neglected in the single-domain state. In order to study the role of anomalously strong nonlinear electrostriction coupling, the “inverted” signs of the linear electrostriction coupling, and the influence of the terms $\gamma P_3^5 + \delta P_3^7$ in Eq. (1) on the pressure effect of the polarization switching in CIPS nanoparticles, in what follows we limit our consideration to the single-domain polarization-switching scenario.

B. Pressure effect on the single-domain polarization-switching scenario

Numerical results presented in the section are obtained and visualized using a specialized software, *Mathematica* 13.1 [47]. The field dependence of a quasistatic single-domain polarization can be found from the following equation:

$$\Gamma \frac{\partial P_3}{\partial t} + \alpha^* P_3 + \beta^* P_3^3 + \gamma P_3^5 + \delta P_3^7 = E. \quad (3)$$

Here, $\beta^*(\sigma_i) = \beta - 4Z_{i33}\sigma_i$ and E is the external field inside the core, whose frequency ω is regarded to be very small, e.g., $\omega\tau \ll 10^{-4}$. The depolarization field, E_d , and stresses, σ_i , contribute to the “renormalization” of coefficient $\alpha(T)$, which becomes the temperature-, stress-, shape-, size-, and screening-dependent function α^* [20]:

$$\alpha^*(T, n_d, \sigma_i) = \alpha(T) + \frac{n_d}{\varepsilon_0[\varepsilon_b n_d + \varepsilon_s(1 - n_d) + n_d(L/\lambda)]} - 2\sigma_i(Q_{i3} + W_{ij3}\sigma_j). \quad (4)$$

The derivation of the second term in Eq. (4) is given in Ref. [48]. Parameters ε_b and ε_s are the background dielectric permittivity [34] of the ferroelectric core and the relative dielectric permittivity of its screening shell or surrounding medium, respectively. Here $\lambda = \lambda(E_d)$, whose value can be rather small due to the surface band bending

induced by the “bare” depolarization field E_{d0} [see details after Eq. (S.5), Appendix A within the Supplemental Material [30]]. If we assume that $\lambda(E_0) \gg L$ and $\varepsilon_s \cong \varepsilon_b$, the estimate $E \approx \varepsilon_s E_0 / (\varepsilon_b n_d + \varepsilon_s(1 - n_d)) \cong E_0$ is valid. The dimensionless parameter n_d is a shape-dependent depolarization factor introduced as [49]

$$n_d(\xi) = \frac{1 - \xi^2}{\xi^3} \left(\ln \sqrt{\frac{1 + \xi}{1 - \xi}} - \xi \right), \quad \xi = \sqrt{1 - \left(\frac{R}{L}\right)^2}. \quad (5)$$

Here ξ is the eccentricity ratio of the ellipsoid, which depends on the dimensionless shape factor R/L . Both shape-driven and size-driven effects are intertwined in Eq. (4), because its second term, $n_d / (\varepsilon_0[\varepsilon_b n_d + \varepsilon_s(1 - n_d) + n_d(L/\lambda)])$, is a complex function of the shape factor R/L (via the factor n_d) and the size L in the polar direction (via the ratio L/λ). The depolarization factor is determined by the shape (i.e., ellipsoid aspect ratio, R/L) only (see, e.g., Fig. S1, Appendix B within the Supplemental Material [30]). For a polarization orientation, shown in Fig. 1, the factor is maximal for a disk ($n_d = 1$), has an intermediate value for a sphere ($n_d = 1/3$), and is very small for a long needle ($n_d \sim (R/L)$) with $P_3 \uparrow \uparrow X_3$. The depolarization factor controls the magnitude of depolarization field, which in turn determines the transition temperatures, phase boundaries and critical sizes of nanoparticles [2,20]. Thus, it is reasonable to consider three main shapes, a disk, a sphere, and a needle, which allow the whole picture of shape-dependent depolarization effects to be imagined.

The diagrams in Figs. 3(a)–3(c) illustrate a typical influence of the hydrostatic pressure, σ , and temperature, T , on the value of spontaneous polarization, P_s , which corresponds to the absolute minimum of the LGD free energy for various phases (or states) of a CIPS nanodisk, nanosphere, and nanoneedle. All diagrams contain a large dark-violet region, where the PE phase with $P_s = 0$ is absolutely stable. As we have shown earlier [20], a part of the dark-violet region located between the dashed white curve and the sharp violet-red boundary contains the metastable FI phase, since CIPS undergoes a first-order FI-PE phase transition at the sharp violet-red boundary. The magnitude of P_s has a jump at the boundary. The PE phase becomes metastable in the region between the dotted white curve and the sharp violet-red boundary, where FI becomes absolutely stable. The dotted and dashed curves are the boundaries of the PE and FI phases’ absolute instability, and the PE and FI phases coexist between these curves. To underline this, we add thin red stripes (i.e., FI metastable and PE absolute stable regions) and violet stripes (i.e., FI absolute stable and PE metastable regions) in the region between dotted and dashed curves.

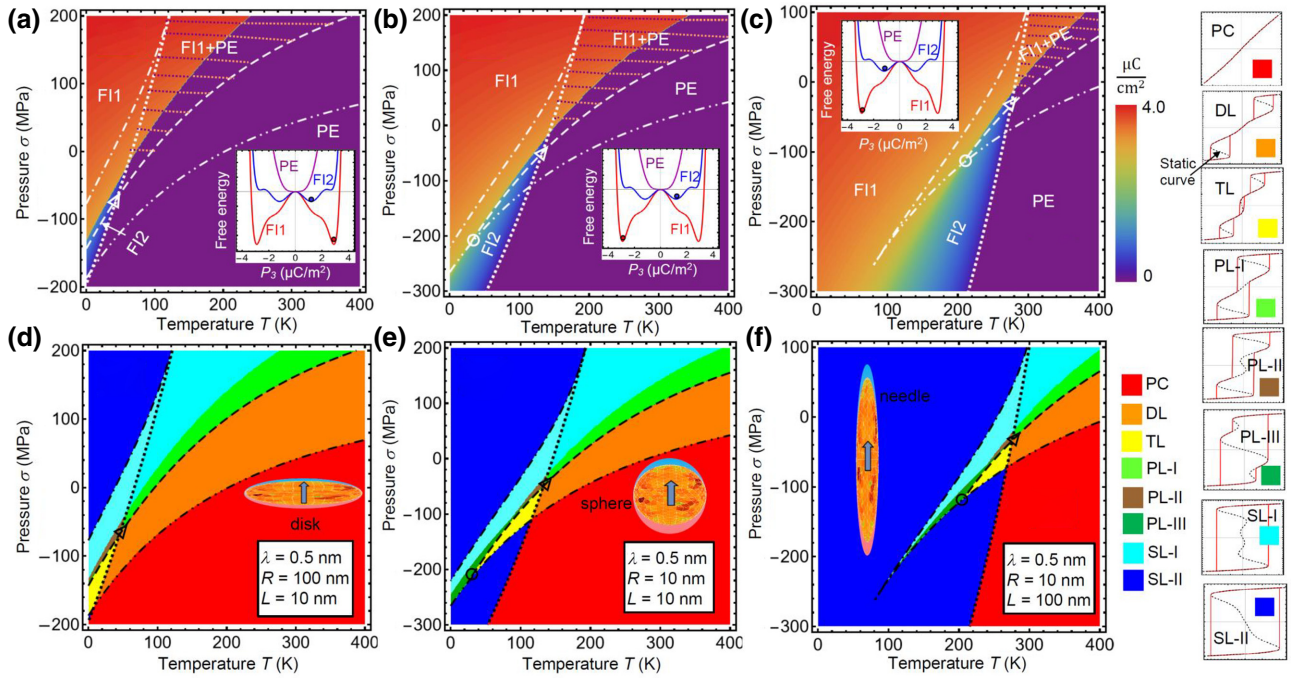


FIG. 3. (a)–(c) The spontaneous polarization, P_s , and (d)–(f) the shape of quasistatic hysteresis loops, $P_3(E)$, calculated as a function of temperature T and pressure σ for the stressed CIPS nanodisk with a radius $R = 100$ nm and a semiheight $L = 10$ nm (a),(d), nanosphere with a radius $R = 10$ nm (b),(e), and nanoneedle with a radius $R = 10$ nm, and semilength $L = 100$ nm (c),(f). Color coding in the diagrams (a)–(c) is the absolute value of P_s in the deepest potential well of the LGD free energy. PE is the paraelectric phase, FI1 and FI2 are ferrielectric states; the CEP is marked by a triangle and the BEP is marked by a circle (see the explanation of abbreviations in the text). Color scale in the diagrams (d)–(f): red is paraelectric curves (PCs), orange is double loops (DLs), yellow is triple loops (TLs), light-green is pinched loops of the first type (PL-I), brown is pinched loops of the second type (PL-II), dark-green is pinched loops of the third type (PL-III), cyan is single loops of the first type (SL-I), and blue is single loops of the second type (SL-II). The static curves are shown as the thin black dashes inside the hysteresis loops in the right column. The screening length $\lambda = 0.5$ nm, surface-tension coefficient $\mu = 0$; CIPS parameters are listed in Table SI within the Supplemental Material [30].

The intersection of the dashed and dotted curves is the CEP, denoted by a triangle in Fig. 3. Phase diagrams, shown in Figs. 3(b) and 3(c), also have the BEP marked by a white circle, which is positioned where the dashed and dot-dot-dashed curves intersect. The dot-dashed and dot-dot-dashed curves separate the region where the static dependences of polarization on the applied electric field (named “static curves”) have four or six turning points; this number defines the structure of quasistatic hysteresis loops of polarization (as described in Appendix B within the Supplemental Material [30]). The static curves, which correspond to zero frequency external field, $\omega = 0$, are shown as the thin black dashes inside the hysteresis loops in the right column (described in more detail below). The quasistatic hysteresis loops are calculated from Eq. (3) for $\omega\tau = 10^{-5}$.

As we have shown earlier [20], the FI phase has two states. The large red region in Figs. 3(a)–3(c) is the ferrielectric state 1 (FI1) with a relatively large P_s , and a small blue region is the ferrielectric state 2 (FI2) with a small P_s . The physical reason for the difference in P_s in FI1 and FI2 states is the structure of four-well potential, schematically

shown in inset to Fig. 3(a). Here the red point in the deepest well of the red curve corresponds to a relatively large P_s in the FI1 state, and the blue point in the deepest well of the blue curve corresponds to a relatively small P_s in the FI2 state. Note that the color scale of P_s corresponds to the deepest potential well of the LGD free energy.

Upon cooling the FI2 state transforms into the FI1 state. For Fig. 3(c) and 3(b), at temperatures below the BEP temperature and pressures smaller than the BEP pressure, a smooth isostructural transition from the FI2 to FI1 states occurs with a continuous increase of P_s . The polarization value, corresponding to the shallower well, is sensitive to the BEP, but it is not shown in Figs. 3(b) and 3(c).

The diagrams in Figs. 3(a)–3(c) can be explained within the pseudospin formalism. The presence of the three-well local potential for the In^{3+} cations in the CIPS lattice determines the observed peculiar shape of the $T - \sigma$ phase diagram with one PE and two ferrielectric (FI1 and FI2) states. The shape of the local potential determines the character of the phase transition from PE to FI states, either a first-order transition with a steplike appearance of P_s or a second-order transition with a continuous increase of

P_3 . The stability of the local potential central well for the In^{3+} cation determines the first-order character of the PE-FI phase transition for $\sigma > 0$. The side well of the In^{3+} cations' local potential is stabilized for $\sigma < 0$, and the second-order PE-FI2 phase transition occurs.

The behavior of the spontaneous polarization across the $T - \sigma$ diagram determines switching peculiarities of the polarization in different regions of the “loop” diagrams shown Figs. 3(d)–3(f). The diagrams in Figs. 3(d)–3(f) illustrate a typical influence of the hydrostatic pressure σ and temperature T on the shape of quasistatic hysteresis loops, $P_3(E)$, calculated for a CIPS nanodisk, nanosphere, and nanoneedle. The diagrams contain a red region of paraelectric curves (PCs), an orange region of double loops (DLs), a yellow region of triple loops (TLs), a light-green region of pinched loops of the first type (PL-I), brown and dark-green regions of pinched loops of the second and third type (PL-II and PL-III), a cyan region of single loops of the first type (SL-I), and a blue region of single loops of the second type (SL-II). These different shapes of the hysteresis loops (red curves) and their corresponding static curves (thin black dashes inside the hysteresis loops) are shown in the right column; their detailed classification is given in Appendix B within the Supplemental Material [30]. The classification takes into account both the loop shape and the structure of the static curves.

The regions of PC and DL, separated by a dot-dot-dashed curve in Figs. 3(d)–3(f), are located inside the PE phase region shown in Figs. 3(a)–3(c). Indeed, the DL can be observed in the PE phase above the first-order transition, as shown by Ishibashi [22]. These loops are related to a first-order phase transition induced by the electric field.

The yellow region of TL in Figs. 3(d)–3(f) is located inside the blue region of the FI2 phase shown in Figs. 3(a)–3(c). TLs fill the triangular region inside the dotted, dashed, and dot-dot-dashed curves in Figs. 3(d)–3(f). The CEP and BEP are two vertices of the triangle. As it follows from the structure of the static curve, a TL can be imagined as the result of superposition of a “central” single loop (corresponding to the switching of the “small” polarization in the FI2 state) and a double loop (corresponding to the switching of a “larger” polarization in the FI2 state). The coexistence of these two polarizations in the four-well FI2 state determines the stability of TL in the yellow triangular region in Figs. 3(d)–3(f).

The shape and transformation of the pinched loops in the light-green (PL-I), brown (PL-II), and dark-green (PL-III) regions in Figs. 3(d)–3(f) are also determined by the temperature and pressure evolution of superposed single and double loops. The region of PL-I is located above the dashed curve in the PE and FI1 coexisting region. Thin strips of PL-II and PL-III regions are located near the diffuse boundary between FI2 and FI1 states. The cyan triangular region of SL-I partially fills the region between the dot-dashed, dot-dot-dashed, and dashed curves in

Figs. 3(d)–3(f). The SL-I region is located inside the FI1 state in Figs. 3(a)–3(c). The SL-I region is also stable in the PE and FI1 coexistence region. The large blue region of SL-II in Figs. 3(d)–3(e) is located inside the FI1 and FI2 states' regions of absolute stability in Figs. 3(a)–3(c). The absolute stability of the FI states appears when the four-well potential transforms into the two-well potential, shown by red curves with a red filled circle in the insets in Figs. 3(a)–3(c).

A common feature of Fig. 3 is the strong anomalous influence of the hydrostatic pressure on the appearance of polarization switching in CIPS nanoparticles, i.e., the unusual shape hysteresis loops and particularly the existence of the wide regions of DL, PL-I, and TL. The strong increase of the polarization-switching region for $\sigma > 0$ and the increase of the hysteresisless region for $\sigma < 0$, is caused by the anomalous temperature dependence and “inverted” sign of the CIPS linear and nonlinear electrostriction coupling coefficients. The unusual shape of the quasistatic single-domain hysteresis loops, including the DL, PL, and TL, is defined by the specific structure of the static curves, which is determined by the eighth-order LGD potential. The above-mentioned properties of polarization switching are common for CIPS nanodisks, nanospheres, and nanoneedles, but there are some distinct features, which are analyzed below.

In the case of CIPS nanodisks, shown in Fig. 3(a), the region of the FI1 state is relatively small and strongly decreases with a temperature increase. Under the expansion pressure of -40 MPa (or greater in magnitude) a very small region of the FI2 state appears and continuously transforms into the PE phase. The FI1-PE and FE1-FE2 phase boundaries are sharp. The PC region prevails in tension-stressed ($\sigma < 0$) nanodisks; the wide SL-II, PL-I, and DL regions prevail for compression-stressed ($\sigma > 0$) nanodisks in the diagram in Fig. 3(d). Four types of loops, namely the PL-II, TL, DL, and PL-I, coexist in the CEP. The PL-II region is almost absent for disks, occupying a very small region at low temperatures and $\sigma < 0$. The PL-III region is absent for disks, at least for the considered parameters, and a small region of TL is located at low temperatures (below 40 K). Since sizeable regions of PL-III and TL loops are required for nonvolatile multibit memory cells [27], CIPS nanodisks do not look promising for advanced memories. Since the wide region of DL are useful for energy storage, CIPS nanodisks may be quite suitable for this application.

In the case of CIPS nanospheres, shown in Fig. 3(b), the region of the FI1 state is much larger compared to the case of nanodisks, shown in Fig. 3(a). Under the expansion pressure of -40 MPa (or greater in magnitude) a relatively wide region of the FI2 state appears and continuously transforms into the PE phase. The first-order FI1-PE phase boundary is sharp, and the FI1-FI2 boundary is sharp above and diffuse (i.e., second order) below

the BEP. Comparing Fig. 3(e) with 3(d), one can see that a thin region of PL-III appears for $\sigma < 0$ in the temperature range from 0 to 100 K. The dominant regions for the case of the nanodisk [Fig. 3(d)] for high temperatures and $\sigma < 0$ is PC and for temperatures lower than 250 K and $\sigma > 0$ is SL-I and SL-II; CEP is present and BEP is absent. For nanospheres [Fig. 3(e)] there are two special points, CEP and BEP, located in the middle of the loop diagram. The SL-II, PL-III, and TL loops coexist in the BEP. The size of the SL region increases compared to the case of the nanodisks. The temperature range of the PL-III and TL regions stability is from 0 to 120 K. The DL are stable from 100 to 400 K. Since relatively large regions of the pressure-induced PL-III, TL, and DL loops are predicted for stressed CIPS nanospheres, they can be promising candidates for energy storage (from 100 to 400 K) and multibit memory cells (from 0 to 120 K).

The diagrams of CIPS nanoneedles, shown in Figs. 3(c) and 3(f), look similar to the diagrams of nanospheres, shown in Figs. 3(b) and 3(e). However, the transition region between FI1 and FI2 states in Fig. 3(c) is wider and shifted toward higher temperatures and pressures in comparison with Fig. 3(b). Due to the size effect, the SL-II region is larger, and the sizes of DL, PL-I, PL-II, PL-III, and TL regions are slightly smaller for nanoneedles than for nanospheres and shifted to significantly higher temperatures [compare Figs. 3(e) and 3(f), respectively]. Indeed, the depolarization-field contribution, given by the term $n_d/(\epsilon_0[\epsilon_b n_d + \epsilon_s(1 - n_d) + n_d(L/\lambda)])$ in Eq. (4), is smaller for nanoneedles with a semilength $L = 100$ nm than for the nanospheres with a radius $R = 10$ nm. The CEP and BEP are shifted to higher temperatures in comparison to the previous case. Since the temperature range of the TL region stability reaches 260 K at $\mu = 0$, which is relatively close to room temperature, CIPS nanoneedles are more promising candidates for multibit memory cells than nanospheres, where the TL region stability reaches 120 K at $\mu = 0$. The stressed CIPS nanoneedles are less promising for energy storage than nanospheres and nanodisks, because the region of DL in Fig. 3(f) is smaller than the region for nanospheres in Fig. 3(e), and much smaller than the DL region for nanodisks in Fig. 3(d). However, it does not mean that CIPS nanoneedles cannot be used in energy storage, because the region of DL in Fig. 3(f) is wide enough and exists in the temperature range (250–400) K.

Next, we analyze the pressure influence on polarization switching at room temperature, since the temperature is a critical parameter for most applications. It is seen from Fig. 4, calculated for a CIPS nanodisk, nanosphere, and nanoneedle, that by varying the sign of applied pressure (from expansion to compression) and its magnitude (from zero to several hundreds of MPa), a quasistatic hysteresisless paraelectric curve can transform into a double, pinched, or single hysteresis loop. The above-mentioned properties of polarization switching

are qualitatively similar for CIPS nanodisks, nanospheres, and nanoneedles at room temperature, but there are some quantitative differences which are analyzed below.

For CIPS nanodisks, the pressure-induced transition from double to single hysteresis loops occurs at relatively high compression pressures [see Figs. 4(a)–4(c) and Fig. S9, Appendix C within the Supplemental Material [30]]. As the pressure increases from 70 to 170 MPa, small double loops grow and become more pronounced, finally merging together into a pinched loop of the first type (PL-I). A further increase of pressure from 170 to 210 MPa leads to a gradual growth of the pinched section width, and the pinched loop finally transforms into a single loop of the second type (PL-II). The two coercive fields of the double loops vary in range (0–60) mV/nm and decrease with an increase in pressure; the coercive field of pinched and single loops increases from 20 to 60 mV/nm with an increase in pressure.

For CIPS nanospheres, the pressure-induced transition from double to pinched hysteresis loops occurs under a pressure increase from 20 to 100 MPa [see Figs. 4(d)–4(f) and Fig. S10, Appendix C within the Supplemental Material [30]]. A further increase of pressure from 100 to 140 MPa leads to a gradual growth of the pinched section, and the pinched loop of the third type (PL-III) eventually transforms into a single loop of the first type (SL-I). The coercive fields for nanospheres are one and a half times smaller than the fields for nanodisks. For CIPS nanoneedles, the pressure-induced transition from double hysteresis loops to pinched loops, and then to single loops, occurs within a much narrower pressure range, from –40 to 10 MPa [see Figs. 4(g)–4(i) and Fig. S11, Appendix C within the Supplemental Material [30]]. The coercive fields for nanoneedles are approximately 2 times smaller than the fields for nanospheres.

Figure 5 shows the onset and temperature evolution of stress-induced PL-III and TL hysteresis loops in CIPS nanoneedles in the temperature range (265–300) K. Under zero surface tension ($\mu = 0$), the TL appears from the PL-III in the temperature range (265–270) K for a pressure $\sigma \cong -50$ MPa, and gradually transforms into a DL near 280 K [see Figs. 5(a)–5(c)]. SL-I and PL-III are stable for stress-free nanoneedles (see Fig. S12, Appendix C within the Supplemental Material [30]). Negative surface tensions, $\mu \cong -(0.7 - 1)$ N/m, induce a TL around 290 K for zero external pressure, $\sigma = 0$ [see Figs. 5(d), 4(f)]. Hence it is possible to shift the $T - \sigma$ range of the PL-III and TL stability to zero stress and room temperature by a small negative surface tension, which shows the CIPS nanoneedles' potential for nonvolatile and/or dynamic multibit memory cells.

The value of the coercive field (in fact, the coercive voltage) is measured in polarization switching experiments. As a rule, the field is directly related with the height of barrier for the case of a single-domain polarization

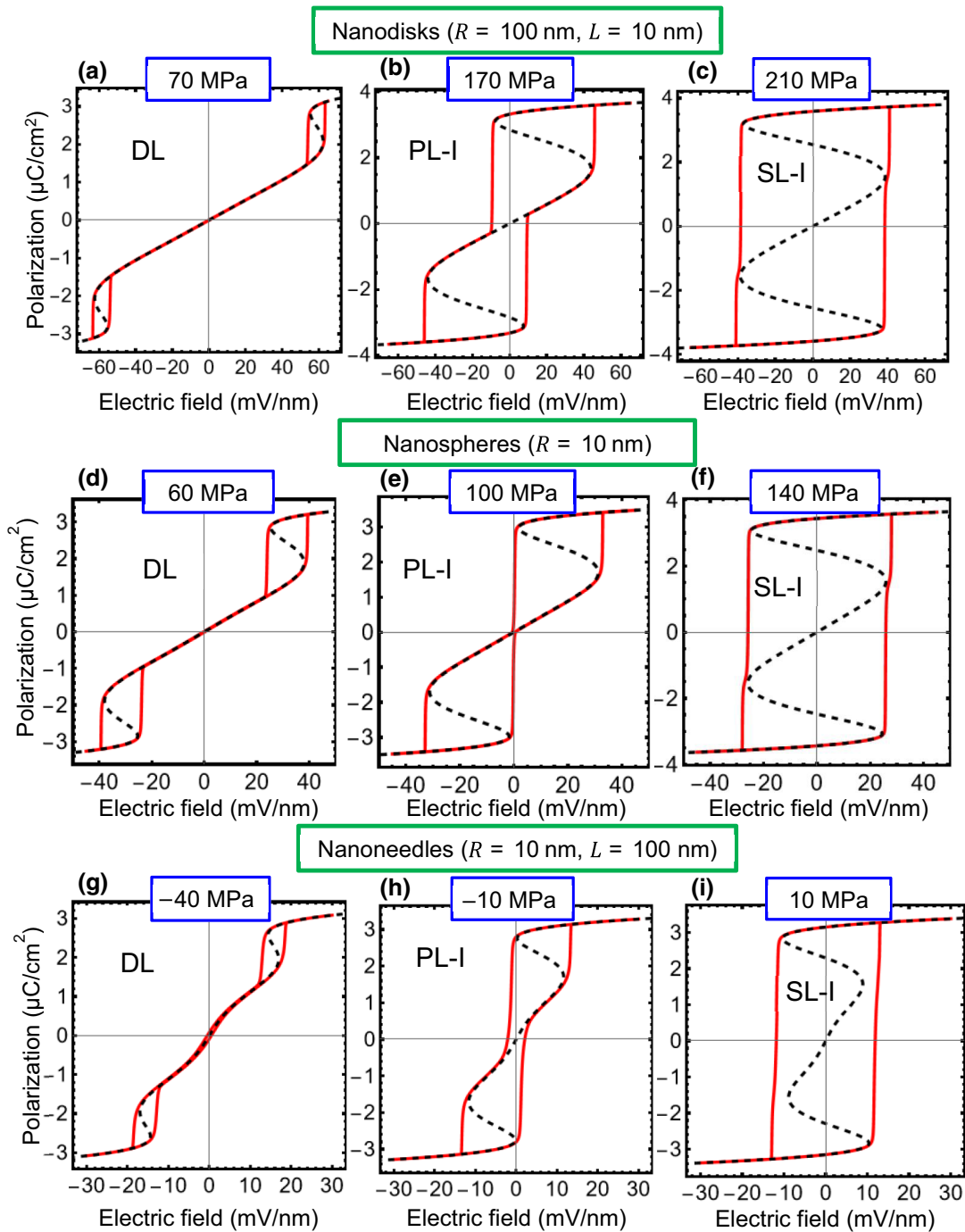


FIG. 4. Electric field dependence of the polarization P_3 , calculated for CIPS nanodisks with $R = 100$ nm, $L = 10$ nm (a)–(c), nanospheres with $R = 10$ nm (d)–(f), and nanoneedles with $R = 10$ nm, $L = 100$ nm (g)–(i), under different hydrostatic pressures: $\sigma = 70$ MPa (a), 170 MPa (b), 210 MPa (c), 60 MPa (d), 100 MPa (e), 140 MPa (f), -40 MPa (g), -10 (h), and 10 MPa (i). Black dashed curves are static dependences and red solid loops are quasistatic hysteresis loops. Temperature $T = 300$ K, screening length $\lambda = 0.5$ nm; other parameters are the same as in Fig. 3.

switching in the case of three-well thermodynamic potential (when the ferroelectric transition is of the first order); or the field is directly related with the depth of potential well for the case of a single-domain polarization switching in the case of two-well thermodynamic potential (when

the ferroelectric transition is of the second order). As a rule, the barrier, estimated from the experimental polydomain polarization switching, is very different from the “phenomenological” switching barrier, as well as from the barrier calculated by density-functional theory (DFT),

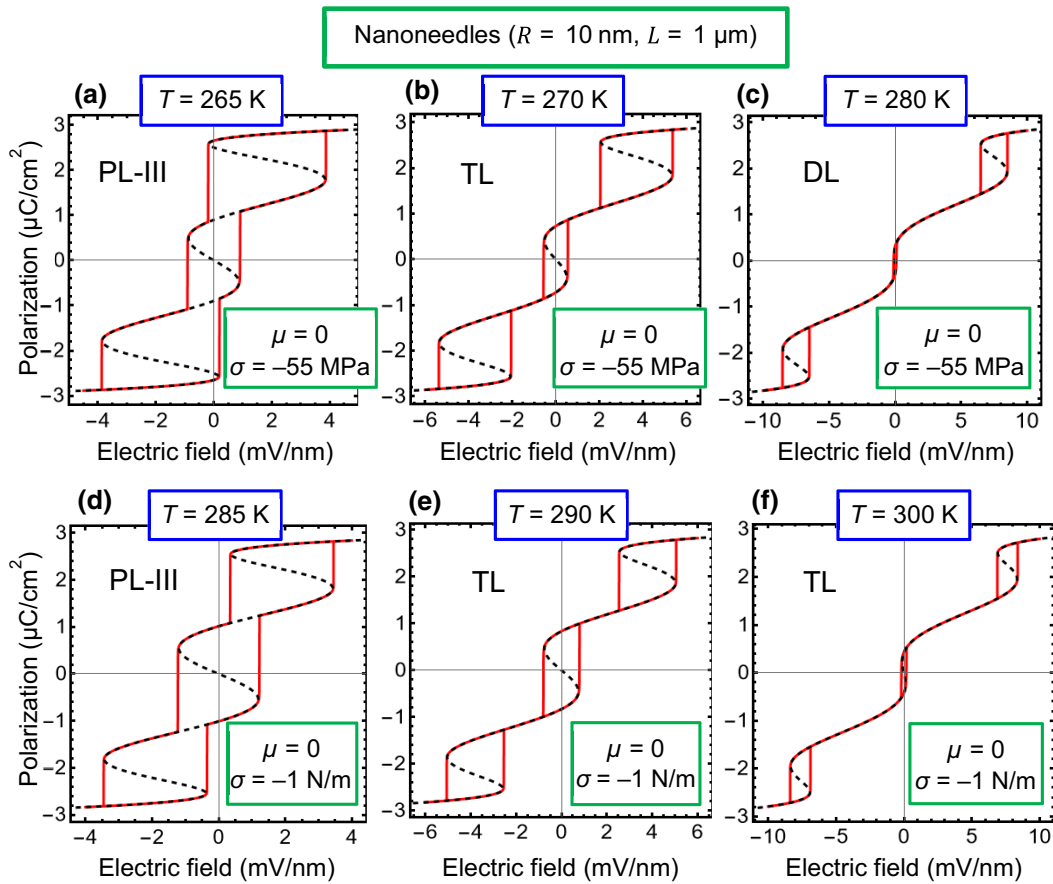


FIG. 5. Electric field dependence of the polarization P_3 , calculated for CIPS nanoneedles with sizes $R = 10$ nm and $L = 1$ μm . Temperature, T , hydrostatic pressure, σ , and surface-tension coefficient, μ , are listed in the legends. Black dashed curves are static dependences and red solid loops are quasistatic hysteresis loops. The screening length $\lambda = 0.5$ nm; other parameters are the same as in Fig. 3.

because the domain formation reduces the depolarization field energy. The phase diagrams of CIPS nanoparticles, shown in Fig. 3, contain the boundaries of the first and the second phase transitions, e.g., FI1-PE and FI2-PE transitions, in dependence on temperature and pressure. Thus, the situation with CIPS nanoparticles is complex, and unlikely the switching barrier calculated within LGD phenomenological approach, which correspond to high temperatures and/or nonzero pressures, can be compared with DFT calculations valid for a bulk or 2D CIPS at low temperatures and zero pressures.

C. Possible applications

We predict that compressed CIPS nanodisks reveal wide temperature and pressure ranges of DL stability in comparison with multiaxial perovskite ferroelectrics, such as BaTiO_3 and PbTiO_3 single crystals. In particular, DL are stable in the temperature range (100–400) K at pressures (0–70) MPa [see Fig. 3(d)]. At zero pressure, the width of the DL region is 100 K, while the width reaches 200 K at $\sigma = 40$ MPa. Hence, compression-stressed CIPS

nanodisks as energy-storage nanomaterials can be competitive with classical antiferroelectrics, such as PbZrO_3 thin films [50]. Indeed, CIPS nanodisks' in-field polarization can reach 4 $\mu\text{C}/\text{cm}^2$, and their thermodynamic coercive field varies in the range (5–50) mV/nm. PbZrO_3 thin films have much higher in-field polarization (approximately 40 $\mu\text{C}/\text{cm}^2$) and also much higher thermodynamic coercive fields (approximately 500 mV/nm). Of course, the stored energy in a CIPS nanoflake [proportional to the area above the DL, see green region in Fig. 6(a)] is much smaller than in a PbZrO_3 thin film, but the losses and writing voltage are also much smaller for CIPS. The region of DL stability for stressed CIPS nanospheres and nanoneedles is smaller than for nanodisks [see Figs. 3(e) and 3(f)], but it is still relatively wide, e.g., 150 K at zero pressure, which is a large value in comparison with most ferroelectrics where the width does not exceed (10–50) K.

Unexpectedly, we predict that stressed CIPS nanospheres and nanoneedles reveal sizeable temperature and pressure ranges of TL and PL-III stability [see Figs. 3(e) and 3(f)], which are very rare in ferroelectrics and

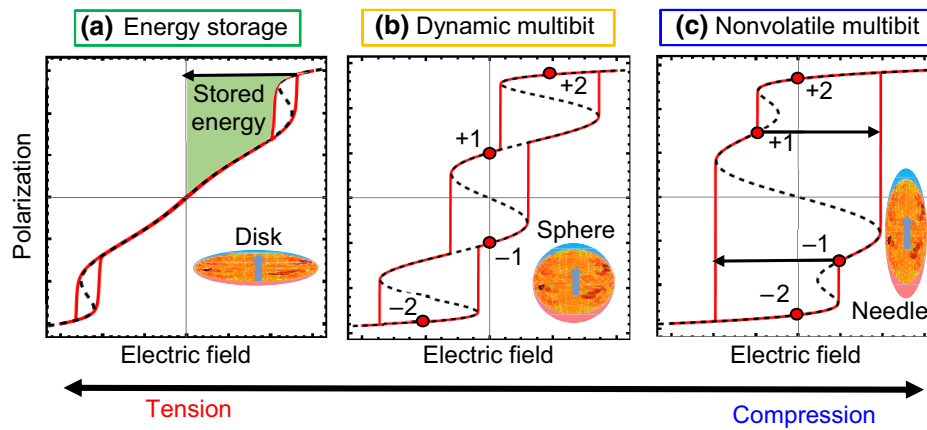


FIG. 6. CIPS nanoparticles for energy storage (a); and dynamic (b) and nonvolatile (c) multibits with memory states ± 1 and ± 2 .

antiferroelectrics. These types of loops can be used for dynamic and/or nonvolatile multibit memory cells, as proposed in Ref. [27] and schematically shown in Figs. 6(b) and 6(c), respectively. The stability of PL-III and TL at zero external stress, room temperature, and relatively small negative surface tension μ makes nanocomposites with CIPS nanoneedles promising for use in dynamic and/or nonvolatile multibit memory cells.

The pressure-induced transition of the hysteresis loops in composites with CIPS nanoparticles can be used in precise pressure sensors for high-pressure applications, such as air compressors or shockwave detectors. The pressure-induced transitions of the polar state and switching scenario in CIPS nanoparticles occur at relatively low pressures (e.g., several MPa) in comparison with other ferroelectrics (approximately GPa), which is quite reasonable for practical applications. This can be useful for high-pressure piezosensors, because this could lead to higher precision of pressure measurements.

We should note, that the experimental verification of our theoretical predictions is still absent, because it is a big challenge to make high-quality ensembles of van der Waals layered chalcogenide nanoparticles in the form of regular ellipsoids with a controllable aspect ratio. However, it is possible to synthesize multilayer CIPS nanoflakes and control the height of the flake by changing the number of layers [51], make nanowires by curling CIPS layers and nanoflakes and controlling their radius and number of layers, as well as to grind multilayer nanoflakes using a ball milling, and then to separate the milled particles by average sizes using nanoporous sieves. From a theoretical standpoint, the nanoflake with a height $2R$ much bigger average lateral size $2L$ can be substituted by a disk-shaped nanoparticle with the accuracy of several percent for $L > 10R$ [20]. The average sizes of milled particles can be considered as “effective” sizes of an ellipsoidal nanoparticle. The accuracy of an “effective” size approach is determined by the scattering of sizes and shapes in the

ensemble, but it is the only way to obtain analytical results using an effective media approach.

IV. CONCLUSIONS

We reveal an unusually strong influence of hydrostatic pressure on the appearance of polarization switching in CIPS nanoparticles, hysteresis loop shape, magnitude of the remanent polarization, and coercive fields, which is explained by the effect of the anomalous temperature dependence and “inverted” sign of CIPS linear and non-linear electrostriction coupling coefficients. In particular, by varying the sign of the applied pressure (from expansion to compression) and increasing its magnitude (from zero to several hundreds of MPa), a quasistatic hysteresisless paraelectric dependence can transform into a double, triple, pinched, or single hysteresis loop. The form of quasistatic hysteresis loops is defined by specific static dependences of polarization on applied electric field, i.e., “static curves.” The structure of the static curves has very specific features for CIPS, since its LGD potential is an eighth-order polynomial in the polarization powers.

Due to the sufficiently wide temperature and pressure ranges of double, triple, pinched, and single hysteresis loop stability (at least in comparison with many other ferroelectric materials), stressed CIPS nanodisks can be of particular interest for applications in energy storage (in the region of double loops), and CIPS nanoneedles and nanospheres can be used in nonvolatile and/or dynamic multibit memory cells (in the region of PL-III and TL loops).

A physical origin of TL loops, which are very rare in ferroelectrics and antiferroelectrics, is the coexistence of “small” and “larger” polarizations in the four-well ferroelectric state. Since the temperature range of the TL region stability is relatively low for nanospheres and close to room temperature for CIPS nanoneedles, the nanoneedles are more promising candidates for multibit

memory cells than nanospheres. The stress control of the polarization switching scenario allows the creation of advanced piezosensors based on nanocomposites with CIPS nanospheres.

ACKNOWLEDGMENTS

A.N.M. acknowledges EOARD project 9IOE063 and related STCU partner project P751a. E.A.E. acknowledges support of the National Academy of Sciences of Ukraine.

AUTHORS' CONTRIBUTION

The research idea belongs to A.N.M. and Yu.M.V. A.N.M. formulated the problem, performed analytical calculations, analyzed results, and wrote the manuscript draft. E.A.E. and M.E.Y. wrote codes; A.N.M. and M.E.Y. prepared figures and Supplemental Material. Yu.M.V. and D.R.E. worked on the results' explanation and manuscript improvement. All co-authors discussed the obtained results.

-
- [1] J. S. Meena, S. M. Sze, U. Chand, and T.-Y. Tseng, Overview of emerging nonvolatile memory technologies, *Nanoscale Res. Lett.* **9**, 526 (2014).
 - [2] A. N. Morozovska, E. A. Eliseev, S. V. Kalinin, Y. M. Vysochanskii, and Petro Maksymovych, Stress-induced phase transitions in nanoscale CuInP_2S_6 , *Phys. Rev. B* **104**, 054102 (2021).
 - [3] C. Chen, H. Liu, Q. Lai, X. Mao, J. Fu, Z. Fu, and H. Zeng, Large-scale domain engineering in two-dimensional ferroelectric CuInP_2S_6 via giant flexoelectric effect, *Nano Lett.* **22**, 3275 (2022).
 - [4] W. Yang, S. Chen, X. Ding, J. Sun, and J. Deng, Reducing threshold of ferroelectric domain switching in ultrathin two-dimensional CuInP_2S_6 ferroelectrics via electrical–mechanical coupling, *J. Phys. Chem. Lett.* **14**, 379 (2023).
 - [5] X. Bourdon, V. Maisonneuve, V. B. Cajipe, C. Payen, and J. E. Fischer, Copper sublattice ordering in layered CuMP_2Se_6 ($M = \text{In, Cr}$), *J. Alloys Compd.* **283**, 122 (1999).
 - [6] A. Belianinov, Q. He, A. Dziaugys, P. Maksymovych, E. Eliseev, A. Borisevich, A. Morozovska, J. Banys, Y. Vysochanskii, and S. V. Kalinin, CuInP_2S_6 Room temperature layered ferroelectric, *Nano Lett.* **15**, 3808 (2015).
 - [7] M. A. Susner, M. Chyasnachyus, M. A. McGuire, P. Ganesh, and P. Maksymovych, Metal thio- and selenophosphates as multifunctional van der Waals layered materials, *Adv. Mater.* **29**, 1602852 (2017).
 - [8] M. Wu and P. Jena, The rise of two-dimensional van der Waals ferroelectrics, *Wiley Interdiscip. Rev.: Comput. Mol. Sci.* **8**, e1365 (2018).
 - [9] F. Liu, L. You, K. L. Seyler, X. Li, P. Yu, J. Lin, X. Wang, J. Zhou, H. Wang, H. He, S. T. Pantelides, W. Zhou, P. Sharma, X. Xu, P. M. Ajayan, J. Wang, and Z. Liu, Room-temperature ferroelectricity in CuInP_2S_6 ultrathin flakes, *Nat. Commun.* **7**, 12357 (2016).
 - [10] M. A. Susner, M. Chyasnachyus, A. A. Puzetzy, Q. He, B. S. Conner, Y. Ren, D. A. Cullen, P. Ganesh, D. Shin, J. W. McMurray, A. Borisevich, P. Maksymovych, and M. A. McGuire, Cation–eutectic transition via sublattice melting in $\text{CuInP}_2\text{S}_6/\text{In}_4/{}^3\text{P}_2\text{S}_6$ van der Waals layered crystals, *ACS Nano* **11**, 7060 (2017).
 - [11] M. Osada and T. Sasaki, The rise of 2D dielectrics/ferroelectrics, *APL Mater.* **7**, 120902 (2019).
 - [12] M. J. Swamyndhan and S. Ghosh, Designing multi-functional two-dimensional layered transition metal phosphorous chalcogenides, *Phys. Rev. Mater.* **5**, 054409 (2021).
 - [13] P. Toledano and M. Guennou, Theory of antiferroelectric phase transitions, *Phys. Rev. B* **94**, 014107 (2016).
 - [14] V. Maisonneuve, V. B. Cajipe, A. Simon, R. Von Der Muhll, and J. Ravez, Ferrielectric ordering in lamellar CuInP_2S_6 , *Phys. Rev. B* **56**, 10860 (1997).
 - [15] Y. M. Vysochanskii, V. A. Stephanovich, A. A. Molnar, V. B. Cajipe, and X. Bourdon, Raman spectroscopy study of the ferrielectric–paraelectric transition in layered CuInP_2S_6 , *Phys. Rev. B* **58**, 9119 (1998).
 - [16] N. Sivadas, P. Doak, and P. Ganesh, Anharmonic stabilization of ferrielectricity in $\text{CuInP}_2\text{Se}_6$, *Phys. Rev. Res.* **4**, 013094 (2022).
 - [17] Ju. Banys, A. Dziaugys, K. E. Glukhov, A. N. Morozovska, N. V. Morozovsky, and Yu. M. Vysochanskii, *Van der Waals Ferroelectrics: Properties and Device Applications of Phosphorous Chalcogenides* (John Wiley & Sons, Weinheim, 2022), pp. 400. ISBN: 978-3-527-35034-6
 - [18] W. Selke and J. Oitmaa, Monte Carlo study of mixed-spin $S = (1/2, 1)$ Ising ferrimagnets, *J. Phys.: Condens. Matter* **22**, 076004 (2010).
 - [19] A. N. Morozovska, E. A. Eliseev, K. Kelley, Yu. M. Vysochanskii, S. V. Kalinin, and P. Maksymovych, Phenomenological description of bright domain walls in ferroelectric–antiferroelectric layered chalcogenides, *Phys. Rev. B* **102**, 174108 (2020).
 - [20] A. N. Morozovska, E. A. Eliseev, Yu. M. Vysochanskii, V. V. Khist, and D. R. Evans, Screening-Induced Phase Transitions in Core-Shell Ferroic Nanoparticles, *Phys. Rev. Mater.* **6**, 124411 (2022).
 - [21] Y. Ishibashi and Y. Hidaka, On an isomorphous transition, *J. Phys. Soc. Jpn.* **60**, 1634 (1991).
 - [22] M. Iwata and Y. Ishibashi, Phenomenological theory in dielectric tunable materials with the tristable states, *Ferroelectrics* **503**, 7 (2016).
 - [23] E. V. Balashova and A. K. Tagantsev, Polarization response of crystals with structural and ferroelectric instabilities, *Phys. Rev. B* **48**, 9979 (1993).
 - [24] C. Y. Lum, K.-G. Lim, and K.-H. Chew, Revisiting the Kittel's model of antiferroelectricity: phase diagrams, hysteresis loops and electrocaloric effect, *J. Phys.: Condens. Matter* **34**, 415702 (2022).
 - [25] I. Zamaraite, R. Yevych, A. Dziaugys, A. Molnar, J. Banys, S. Svirskas, and Yu Vysochanskii, Double Hysteresis Loops in Proper Uniaxial Ferroelectrics, *Phys. Rev. Appl.* **10**, 034017 (2018).

- [26] I. Suzuki and K. Okada, Phenomenological theory of anti-ferroelectric transition. IV. Ferrielectric, *J. Phys. Soc. Jpn.* **45**, 1302 (1978).
- [27] L. Baudry, I. Lukyanchuk, and V. M. Vinokur, Ferroelectric symmetry-protected multibit memory cell, *Sci. Rep.* **7**, 42196 (2017). <https://www.nature.com/articles/srep42196.pdf>.
- [28] J. Mangeri, Y. Espinal, A. Jokisaari, S. P. Alpay, S. Nakhmanson, and O. Heinonen, Topological phase transformations and intrinsic size effects in ferroelectric nanoparticles, *Nanoscale* **9**, 1616 (2017).
- [29] F. Seitz, H. Ehrenreich, and D. Turnbull, *Solid State Physics* (Academic Press, New-York, 1996), pp. 80–150.
- [30] See Supplemental Material at <http://link.aps.org/supplemental/10.1103/PhysRevApplied.19.054083> for a mathematical formulation of the problem, a table of material parameters, a description of methods, and numerical algorithms.
- [31] L. D. Landau and I. M. Khalatnikov, On the anomalous absorption of sound near a second order phase transition point, In *Dokl. Akad. Nauk SSSR* **96**, 496 (1954).
- [32] Yu. M. Vysochanskii, M. M. Mayor, V. M. Rizak, V. Yu. Slivka, and M. M. Khoma, The tricritical Lifshitz point on the phase diagram of $\text{Sn}_2\text{P}_2(\text{Se}_x\text{S}_{1-x})_6$, *Soviet, J. Exp. Theor. Phys.* **95**, 1355 (1989).
- [33] A. Kohutych, R. Yevych, S. Perechinskii, V. Samulionis, J. Banys, and Yu. Vysochanskii, Sound behavior near the Lifshitz point in proper ferroelectrics, *Phys. Rev. B* **82**, 054101 (2010).
- [34] A. K. Tagantsev and G. Gerra, Interface-induced phenomena in polarization response of ferroelectric thin films, *J. Appl. Phys.* **100**, 051607 (2006).
- [35] P. Guranich, V. Shusta, E. Gerzanich, A. Slivka, I. Kuritsa, and O. Gomonnai, Influence of hydrostatic pressure on the dielectric properties of CuInP_2S_6 and $\text{CuInP}_2\text{Se}_6$ layered crystals, *J. Phys.: Conf. Ser.* **79**, 012009 (2007).
- [36] A. V. Shusta, A. G. Slivka, V. M. Kedylich, P. P. Guranich, V. S. Shusta, E. I. Gerzanich, I. P. Prits, Effect of uniaxial pressure on dielectric properties of CuInP_2S_6 crystals. Scientific Bulletin of Uzhhorod University. Physical Series, **28**, 44 (2010).
- [37] A. Molnar, K. Glukhov, M. Medulych, D. Gal, H. Ban, and Yu. Vysochanskii, in *Abstract book of the FMNT 2020 Online Conference, Virtual Vilnius, Lithuania, 23–26 November* (2020).
- [38] A. Kohutych, V. Liubachko, V. Hryts, Yu. Shiposh, M. Kundria, M. Medulych, K. Glukhov, R. Yevych, and Yu. Vysochanskii, Phonon spectra and phase transitions in van der Waals ferroics $\text{MM}'\text{P}_2\text{X}_6$, *Mol. Cryst. Liq. Cryst.* **747**, 14 (2022).
- [39] J. Banys, J. Macutkevicius, V. Samulionis, A. Brilingas, and Yu. Vysochanskii, Dielectric and ultrasonic investigation of phase transition in CuInP_2S_6 crystals, *Phase Transitions* **77**, 345 (2004).
- [40] V. Samulionis, J. Banys, Yu. Vysochanskii, and V. Cajipe, Elastic and electromechanical properties of new ferroelectric-semiconductor materials of $\text{Sn}_2\text{P}_2\text{S}_6$ family, *Ferroelectrics* **257**, 113 (2001).
- [41] A. N. Morozovska, M. D. Glinchuk, and E. A. Eliseev, Phase transitions induced by confinement of ferroic nanoparticles, *Phys. Rev. B* **76**, 014102 (2007).
- [42] V. A. Shchukin and D. Bimberg, Spontaneous ordering of nanostructures on crystal surfaces, *Rev. Mod. Phys.* **71**, 1125 (1999).
- [43] Wenhui Ma, Surface tension and Curie temperature in ferroelectric nanowires and nanodots, *Appl. Phys. A* **96**, 915 (2009).
- [44] V. Ya. Shur, E. L. Rumyantsev, D. V. Pelegov, V. L. Kozhevnikov, E. V. Nikolaeva, E. L. Shishkin, A. P. Chernykh, and R. K. Ivanov, Barkhausen jumps during domain wall motion in ferroelectrics, *Ferroelectrics* **267**, 347 (2002).
- [45] P. Marton, Discretisation originated Peierls–Nabarro barriers in simulations of ferroelectrics, *Phase Transitions* **91**, 959 (2018).
- [46] E. A. Eliseev, Y. M. Fomichov, S. V. Kalinin, Yu. M. Vysochanskii, P. Maksymovich, and A. N. Morozovska, Labyrinthine domains in ferroelectric nanoparticles: Manifestation of a gradient-induced morphological phase transition, *Phys. Rev. B* **98**, 054101 (2018).
- [47] The *Mathematica* (<https://www.wolfram.com/mathematica>) notebook, which contain the codes, is available at <https://notebookarchive.org/2023-02-8sdtltx>.
- [48] E. A. Eliseev, A. V. Semchenko, Y. M. Fomichov, M. D. Glinchuk, V. V. Sidsky, V. V. Kolos, Yu. M. Pleskachevsky, M. V. Silibin, N. V. Morozovsky, and A. N. Morozovska, Surface and finite size effects impact on the phase diagrams, polar and dielectric properties of $(\text{Sr}, \text{Bi})\text{Ta}_2\text{O}_9$ ferroelectric nanoparticles, *J. Appl. Phys.* **119**, 204104 (2016).
- [49] L. D. Landau, E. M. Lifshitz, and L. P. Pitaevskii, *Electrodynamics of Continuous Media*, 2nd ed. (Butterworth-Heinemann, Oxford, 1984).
- [50] A. N. Morozovska, E. A. Eliseev, A. Biswas, N. V. Morozovsky, and S. V. Kalinin, Effect of Surface Ionic Screening on Polarization Reversal and Phase Diagrams in Thin Antiferroelectric Films for Information and Energy Storage, *Phys. Rev. Appl.* **16**, 044053 (2021).
- [51] L. Chen, Y. Li, C. Li, H. Wang, Z. Han, He Ma, G. Yuan, L. Lin, Z. Yan, X. Jiang, and J.-M. Liu, Thickness dependence of domain size in 2D ferroelectric CuInP_2S_6 nanoflakes, *AIP Adv.* **9**, 115211 (2019).